ECCM

20

26-30 JUNE

2022

LAUSANNE

SWITZERLAND

Proceedings of the 20th European Conference on Composite Materials

COMPOSITES MEET SUSTAINABILITY

Vol 3 – Characterization

Editors : Anastasios P. Vassilopoulos, Véronique Michaud

Organized by :

EPFL

Under the patronage of :

CCLAB Composite Construction Laboratory

LPAC Laboratory for Processing of Advanced Composites

ESCM EUROPEAN SOCIETY FOR COMPOSITE MATERIALS

ECCM 20
26-30 JUNE 2022
LAUSANNE SWITZERLAND

EPFL CCLAB Composite Construction Laboratory LPAC Laboratory for Processing of Advanced Composites

Proceedings of the 20th European Conference on Composite Materials ECCM20 26-30 June 2022, EPFL Lausanne Switzerland

Edited By :

Prof. Anastasios P. Vassilopoulos, CCLab/EPFL
Prof. Véronique Michaud, LPAC/EPFL

Oragnized by:

Composite Construction Laboratory (CCLab)
Laboratory for Processing of Advanced Composites (LPAC)
Ecole Polytechnique Fédérale de Lausanne (EPFL)

ISBN: 978-2-9701614-0-0
DOI: http://dx.doi.org/10.5075/epfl-298799_978-2-9701614-0-0

Published by :

Composite Construction Laboratory (CCLab)
Ecole Polytechnique Fédérale de Lausanne (EPFL)
BP 2225 (Bâtiment BP), Station 16
1015, Lausanne, Switzerland

https://cclab.epfl.ch

Laboratory for Processing of Advanced Composites (LPAC)
Ecole Polytechnique Fédérale de Lausanne (EPFL)
MXG 139 (Bâtiment MXG), Station 12
1015, Lausanne, Switzerland

https://lpac.epfl.ch

Cover:

Swiss Tech Convention Center
© Edouard Venceslau - CompuWeb SA

Cover Design:

Composite Construction Laboratory (CCLab)
Ecole Polytechnique Fédérale de Lausanne (EPFL)
Lausanne, Switzerland

©2022 ECCM20/The publishers

The Proceedings are published under the CC BY-NC 4.0 license in electronic format only, by the Publishers.

The CC BY-NC 4.0 license permits non-commercial reuse, transformation, distribution, and reproduction in any medium, provided the original work is properly cited. For commercial reuse, please contact the authors. For further details please read the full legal code at http://creativecommons.org/licenses/by-nc/4.0/legalcode

The Authors retain every other right, including the right to publish or republish the article, in all forms and media, to reuse all or part of the article in future works of their own, such as lectures, press releases, reviews, and books for both commercial and non-commercial purposes.

Disclaimer:

The ECCM20 organizing committee and the Editors of these proceedings assume no responsibility or liability for the content, statements and opinions expressed by the authors in their corresponding publication.

ECCM 20
26-30 JUNE 2022
LAUSANNE SWITZERLAND

Hosting Organizations

Composite Construction Laboratory (CCLab)
Laboratory for Processing of Advanced Composites (LPAC)
Ecole Polytechnique Fédérale de Lausanne (EPFL)

Venue

Swiss Tech Convention Center (https://www.stcc.ch)

Conference Chairs

Chair : Prof. Anastasios P. Vassilopoulos, EPFL, Switzerland
Co-Chair: Prof Véronique Michaud, EPFL, Switzerland

International Scientific Committee

Prof. Malin Åkermo SE
Dr. Emmanuel Baranger FR
Prof. Christophe Binetruy FR
Prof. Pedro Camanho PT
Prof. Konstantinos Dassios GR
Prof. Brian Falzon UK
Prof. Kristofer Gamstedt SE
Prof. Sotiris Grammatikos NO
Prof. Christian Hochard FR
Prof. Marcin Kozlowski PL
Prof. Stepan Lomov BE
Dr. David May DE
Prof. Stephen Ogin UK
Prof. Gerald Pinter AT
Prof. Silvestre Pinho UK
Prof. Yentl Swolfs BE
Dr. Julie Teuwen NL
Dr. Panayota Tsotra CH
Prof. Wim van Paepegem BE
Prof. Dimitrios Zarouchas NL
Dr. Andrey Aniskevich LV
Prof. Christian Berggreen DK
Dr. Nicolas Boyard FR
Prof. Valter Carvelli IT
Prof. Klaus Drechsler DE
Prof. Bodo Fiedler DE
Dr. Nathalie Godin FR
Prof. Roland Hinterholzl AT
Prof. Ian Kinloch UK
Dr. Thomas Kruse DE
Prof. Theodoros Loutas GR
Prof. Veronique Michaud CH
Prof. Alessandro Pegoretti IT
Prof. Joao Ramoa Correia PT
Prof. Jose Sena-Cruz PT
Prof. Antonio T. Marques PT
Prof. Thanasis Triantafillou GR
Prof. Albert Turon ES
Prof. Anastasios P. Vassilopoulos CH
Prof. Martin Fagerström SE
Dr. Alexandros Antoniou DE
Prof. Lars Berglund SE
Prof. Michal Budzik DK
Prof. Lucas Da Silva PT
Dr. Andreas Endruweit UK
Prof. Mariaenrica Frigione IT
Dr. Larissa Gorbatikh BE
Dr. Martin Hirsekorn FR
Prof. Vassilis Kostopoulos GR
Prof. Jacques Lamon FR
Prof. Staffan Lundstrom SE
Prof. Peter Mitschang DE
Dr. Soraia Pimenta UK
Prof. Paul Robinson UK
Dr. Olesja Starkova LT
Prof. Sofia Teixeira de Freitas NL
Dr. Stavros Tsantzalis GR
Prof. Danny van Hemelrijck BE
Prof. Michele Zappalorto IT
Dr. Miroslav Cerny CZ

Local Organizing Committee

Prof. Anastasios P. Vassilopoulos, EPFL
Prof. Véronique Michaud, EPFL
Angélique Crettenand and Mirjam Kiener, Lausanne Tourisme
And all those who helped, colleagues who reviewed abstracts and chaired sessions, and CCLab and LPAC students and collaborators who worked hard to make this conference a success.

Contents

Implementing structural fuses in CFRP components via microstructurally-engineered crack paths . . 1

Fractography of polymer composites: future advances 9

Study on the mechanical behaviors of 3D printed hybrid composites with various combination patterns between carbon fiber and glass fiber 17

Effect of weaving patterns on the wettability and mechanical properties of 3D woven i-beam composites 25

Damage characterization in multidirectional glass fibre reinforced polypropylene laminates under quasi-static loading: experiment & simulation 32

Investigating the effect of silane coupling agent on glass fibre/thermoplastic interfacial adhesion . . 40

Hybridisation and chemical treatments applied on carbon and flax fibre reinforced composites . . . 48

Manufacturing and mechanical characterisation of advanced re-formable fibre reinforced vitrimer composites 56

Experimental study on the mechanical behaviour of carbon-fibre z-pin reinforced curved composite laminates under four-point bending 63

Effects of stacking sequences on the interlaminar shear strength of CF/PEKK composites 69

Test methods for dynamic characterization of polymer-based composite materials 75

Characterisation of orthotropic electrical conductivity of unidirectional c/PAEK thermoplastic composites 83

Mechanical characterization of hot compacted self-reinforced polypropylene laminates in comparison with CURV 92

Effect of hybridization on the failure mechanisms of thin/thick hybrid carbon/glass fiber-reinforced composites under flexural loading 98

How do we define and measure strength of a composite? 106

Development of advanced composites through surface characterization of fibers and fillers by inverse gas chromatography 116

Experimental and numerical analysis of heat dissipation in hybrid carbon/glass thin-ply composites for multifunctional applications 122

Development of glass fiber/talc-filled polypropylene composites for use in multilayer sewage pipes application 129

The effect of polymeric matrix type on the thermomechanical performance and synergy of carbonaceous hybrid nanocomposites 136

Glass-fiber reinforced polyurethane foam composite manufactured by long fiber injection process LFI: lightweight potential investigations through mechanical properties and micro-structure characterization 144

The effect of graphene-based materials in polyamide 6 obtained by in situ thermoplastic resin transfer moulding (t-RTM) polymerization 152

An investigation into the performance of aligned, discontinuous carbon fibre composites produced with high performance discontinuous fibre (HIPERDIF) 3G 160

Design of a bending experiment for mechanical characterisation of pultruded rods under compression 167

Mechanical testing of 3D composites – a route to best practice 173

Tapered geometry for testing continuous fiber reinforced thermoplastics under tension 181

Numerical and digital image correlation based experimental analysis of the deformation behaviour of stitched unidirectional continuous carbon fibre/epoxy composites with different stitch patterns under tensile loading 189

Comparison of interlaminar and interfacial shear strength with recycled carbon fiber 197

Experimental investigation of shielding effectiveness of carbon/epoxy composite materials with varying configurations 204

Interfacial shear strength of flax fibre with sustainable matrices 212

Novel z-pin technologies for through thickness reinforcements 219

Temperature dependence of thermophysical properties of carbon/polyamide composite 224

Integrative material characterization of crystalline nanocellulose reinforced filaments for fused-filament fabrication 232

Experimental analysis of glass fibre reinforced nylon-66 under combined tension-torsion loading at low and high rates of strain 240

Tensile characterisation of HIPERDIF PLA/carbon fibre tape under processing conditions 248

Damage delay mechanisms in nanoparticle interleaved composite interfaces 255

Experimental characterisation of electrical conductivities of carbon/epoxy laminates 265

Experimental investigation and simulation of the intra-ply shear property for the unidirectional prepreg forming 273

The effects of interleaf architecture on composite toughness 281

Process simulation of carbon fiber reinforced polyamide 6/metal-hybrid laminates 290

Investigation and characterization of thermal properties of a metal matrix composite reinforced with a metallic glass foam (NI60NB20TA20) 298

Tensile strength of carbon fiber tow/epoxy composites with respect to the microstructure of carbon fiber tow 306

Understanding the influence of local defects on the tensile behavior of sic/sic filament wound tubes from a unidirectional composite model 312

Characterization of damage of a laminated composite with a barrier layer under thermomechanical loading 320

Multi-scale investigation of the effect of sizing chemistry on adhesion and interfacial properties of glass fibres-reinforced epoxy composites 328

Optimisation of microwave-assisted acid digestion conditions for volume fraction measurements of hard to digest fibre-reinforced polymer composites 336

Mechanical properties of the epoxy resin and carbon fibre-reinforced composites modified by core-shell rubber particles . . . 344

On the experimental and numerical characterisation of uncured prepreg composite . . . 352

Identifying microstructural features in unidirectional composite tapes . . . 358

Experimental study of off-axis composite laminates subjected to dynamic compression : the open hole effect . . . 364

Light-weight new generation of graphene/polymer nanocomposites for hydrogen storage . . . 367

Experimental and numerical validation of an inter-ply friction model for thermoset based fibre metal laminates under hot-pressing conditions . . . 374

Thermomechanical characterization of 3D interlock carbon composites . . . 382

Permanent deformation and stiffness degradation of open hole glass/PA6 UD laminates in tension and compression . . . 385

Composite prepregs tack change along the process chain . . . 393

Surface energy determination of particles used as fillers in polymers: application to lignin/PLA composites . . . 401

Simulating PID for curing in a diaphragm forming station . . . 409

A cassette-like peeling test system for evaluating the delamination resistance of soft-to-rigid bonding assemblies . . . 417

Influence of the trigger geometry on the crash behavior of a carbon fiber laminate . . . 423

Residual stress and strain in rapidly cured composites . . . 431

Measurement of damage growth in ultrasonic spot welded joints . . . 439

Comparison of pulsed, pulse-phase, lock-in and standard deviation thermography techniques for non-destructive evaluation of composite materials . . . 448

Surface and subsurface damage assessment of multi-directional composite laminates utilizing a full field imaging technique . . . 454

Multimodal NDT monitoring of textile reinforced cementitious composite sandwich beams in bending 461

Shearography non-destructive testing of a composite ship hull section subjected to multiple impacts 469

Assessment of complex structural scale composite structures by adapting thermoelastic stress analysis for 3D perspective imaging . . . 475

Assessing porosity morphology in composite materials by analysis of ultrasonic analytical signal features . . . 483

Application of machine learning methods on the defect detection in shearographic images . . . 492

Termination criteria for fatigue tests of endless fiber reinforced polymers . . . 502

Weak-bond detection in single-lap shear bonds by evaluating vibroacoustic modulations with artificial neural networks . . . 509

A computational study of acoustic emission due to fiber break and fiber matrix DEBONDING in model composite . . . 517

Study on predicting conductivity of oriented silver nanowires-polydimethylsiloxane composites via terahertz time domain spectroscopy . . . 525

Non-destructive testing of carbon fibre non-woven using novel anisotropic eddy current analysis . . 532

Self-powered structural health monitoring of novel thermoelectric energy harvesting GFRP composites 540

Detection of micro delamination in glass fiber reinforced polymer composites using terahertz wave with convolution neural network . . . 548

Non-destructive evaluation for crystallinity and moisture content of polyethylene terephthalate using pulsed terahertz wave . . . 554

Characterisation of experimental lamb waves propagation in CFRP laminates with the method of wavelet transform . . . 560

Applications of Raman spectroscopy on carbon-based composites . . . 568

Study on predicting electrical conductivity and percolation threshold of multi-walled carbon nanotube/epoxy composites using terahertz time domain spectroscopy . . . 574

Non-destructive evaluation of interfacially engineered composites . . . 580

Development of a new methodology for automated quantification of impact induced damage pattern in CFRP measured by IRT and x-ray radiography . . . 588

Investigation of bamboo nodes structural characteristics with x-ray micro-ct imaging . . . 596

Analysis of crack path transitions in mode I loaded UD carbon fibre composites using in situ 3D computed tomography and the extended finite element method . . . 604

Fibre stress concentrators caused by fibre ends in short aligned glass fibre composites . . . 612

Detailed micro computed tomography investigation of damage progression in notched CFRP specimens . . . 620

Analysis of voids in filament wound composites using a machine-learning-based segmentation tool 628

The role of matrix boundary in the microstructure of unidirectional composites . . . 636

Detailed microstructure characterisation of 3D printed carbon-fibre/PEEK using x-ray computed tomography . . . 644

Micro-computed tomography for mesoscale analysis of woven fibre-reinforced composites . . . 652

Microscale 3D strain mapping at fiber-matrix interface using synchrotron computed tomography and digital volume correlation . . . 660

Electrical impedance tomography for damage detection and localization on carbon fibre reinforced polymer composites . . . 666

Creation of digital material twin (DMT) geometric models of high performance composites based on x-ray microtomography . . . 674

Evaluation of porosity using through-thickness ultrasound and x-ray tomography for out-of-autoclave cured CFRP laminates . . . 682

Coupling rheometry and computed tomography to study the evolution of voids during the consolidation of c/PEKK composites . . . 690

Translaminar fracture of thin-ply composites: a novel design for 4D synchrotron computed tomography . . . 696

Development of the ASTM D8336 21: standard test method for characterizing tack of prepregs using a continuous application and peel procedure . . . 702

Comparing local fiber angles from draping experiments to simulations . . . 710

Experimental characterization of transverse fabric compressibility by means of in-situ-impregnation 718

Measurement of textile compaction response and out-of-plane permeability: 2nd international benchmarking exercise . . . 726

Determination of a racetracking pass-fail criterion for edge flow permeability measurement . . . 733

First insights from the virtual permeability benchmark on a fibrous microstructure . . . 741

Failure of composite laminates under fatigue loading: a focus on the effect of matrix damage on residual strength . . . 749

Global sensitivity analysis of an s-n curve-based fatigue cohesive zone model and validation through a benchmark test . . . 757

Fatigue life study of laminated composites carbon-epoxy manufactured from unidirectional plies and 2D-woven plies combining thermo-mechanical analysis and a residual strength model . . . 765

Fatigue damage and life prediction of unidirectional composites in tension-tension loading . . . 769

Fatigue response of carbon/epoxy laminates under multiaxial stresses for different lay-up parameters 775

Creep-fatigue interaction damage model for GFRP laminates based on thermodynamics . . . 783

Life time estimation of 3D-printed continuous fibre reinforced parts under fatigue loading . . . 791

Fatigue characterisation and monitoring in 3D printed short fibres reinforced polyamide . . . 798

Progressive damage accumulation process of CFRP cross-ply laminates during the early fatigue life . 806

Toward the prediction of the fatigue lifetime of laminated composites, using an incremental damage model with observable variables . . . 813

Fatigue life prediction of GFRP laminates using progressive damage modeling considering viscoelastic behavior . . . 821

Probabilistic fatigue life model of composite laminas under cycle loading . . . 830

Fatigue behavior of continuous-discontinuous sheet molding compounds under application related loading conditions . . . 838

Tensile and flexural fatigue lives of unidirectional CF/PP composites . . . 845

Experimental investigation on fatigue damage growth in thin-ply open-hole composite laminates under tension . . . 853

Influence of viscoelasticity on fatigue behaviour of short fibre reinforced polymers depending on mean stress and fibre orientation . . . 861

Characterization of fatigue crack initiation and propagation in thermoplastic-based hybrid laminates 869

Micro-fatigue test - a new dimension towards a cyclic loading test for interface characterisation . . 877

Fatigue behavior of glass fiber reinforced composite laminates based on recycled pet 883

Experimental and numerical analysis of post-buckling delamination of composite plate under fatigue loads 890

Impact of curing on residual stresses formation and fatigue behaviour of carbon/epoxy laminate composites – application for racing yachts 898

Fatigue characterization of glass fibre/bio based thermoset composite intended for offshore renewable energy applications 905

Mechanical characterization of highly thermo-oxidized reinforced thermoplastic and fatigue life predictions using a through process modeling tool 913

Thermomechanical analysis of the high cycle fatigue behavior of a PEEK CF30 for compressive loadings 921

Static and fatigue behavior of bonded, bolted and hybrid FRP joints 926

Evaluation of the inter laminar shear fatigue damage progression of 3D woven composites with time-lapse x-ray computed tomography 934

Fatigue delamination growth of CFRPS modified with electrospun bis-maleimide resin under mode I remote loading conditions 946

Progressive fatigue damage detection and assessment in composite specimens using random vibration response signals 954

Helicoidal layups and interleaved hybrids: a novel design methodology for impact resistant composite structures 962

Analyses of time-dependent damage within carbon woven-ply reinforced thermoplastic composites laminates at high temperature 969

Mechanical characterization and damage tolerance of 3D-printed coextruded continuous carbon-fiber thermoplastic 977

In-situ full-field measurements for 3D printed composites undergoing interlayer delamination . . . 983

Impact damage tolerance of thermoset composite with hybrid yarns: advanced manufacturing process 991

Experimental investigation on bearing behavior and failure mechanism of hybrid thin/thick-ply composite laminates 999

Assessment of aluminum foils interleaving on the cryogenic impact response of CFRPS: cross-ply, thin-ply and hybrid configurations 1007

Impact performance of out of die UV cured pultruded profiles for vessel structures 1015

Hygrothermal interfacial degradation of flax fibre micro-composites using micro-droplet test 1023

Non-dried flax fibre reinforced thermoplastic composites in wet environments 1031

Damage tolerant thin-ply Bouligand CFRP structures 1039

Accelerated ageing and moisture absorption in polymer composites 1040

Micro-damage and ultimate failure analysis of hybrid thin-ply carbon/glass laminates 1048

The effect of filament winding parameters on damage evolution in carbon fiber reinforced plastic for high-pressure hydrogen vessels . . . 1055

Influence of kerosene flame on in situ mechanical properties of hybrid fibers reinforced PEEK composite laminates . . . 1061

Comparison of glass and carbon long fiber-reinforced polyamide 6 concerning the influence of hydrothermal aging on the mechanical properties . . . 1071

Statistical life prediction of unidirectional CFRP under creep tension load by accelerated testing methodology . . . 1079

Effect of water sorption in neat poly(ether ketone ketone) and its carbon fiber reinforced composite 1087

Development of a test rig for the temperature-dependent determination of composite material properties at cryogenic temperatures . . . 1094

Investigation of mode I fracture toughness of carbon reinforced polymers at cryogenic temperatures 1102

Effort reduction of structural health monitoring in additive manufactured structures by total electrical resistance measurements . . . 1110

Cure monitoring of carbon fiber reinforced polymers using a specific impedancemetry method . . . 1118

Flexural toughening of wave shaped short plastic fibers in a cementitious mortar . . . 1126

Influence of manufacturing procedure on mechanical properties of continuous fiber reinforced thermoplastics . . . 1132

Automated multi-NDT method . . . 1140

Effect of aeronautic fluid Skydrol on neat poly(ether ketone ketone) and its carbon fiber reinforced composite . . . 1146

Braiding characterisation and optimisation: complex geometries . . . 1152

Explicit modelling of matrix damage in a laminated composite ? comparison between linear fracture mechanic and cohesive zone model . . . 1159

Building and characterization of symmetric structural battery . . . 1169

Development of sustainable continuous carbon fiber reinforced polymers . . . 1175

Thermal stability of ELIUM® resin and its composites . . . 1181

Study on the tensile behavior of the tubular braided composite reinforcements . . . 1189

Mechanical characterisation of some polymers used in 3D printing . . . 1196

STXM: nanoscale 2D/3D chemical imaging . . . 1204

INVESTIGATION AND CHARACTERIZATION OF THERMAL PROPERTIES OF A METAL MATRIX COMPOSITE REINFORCED WITH A METALLIC GLASS FOAM (NI60NB20TA20)

Kerstin Dittmann[a], Anna Trauth[a], Kay Weidenmann[a]

a: Institute of Materials Resource Management (MRM), Augsburg University,
Am Technologiezentrum 8, 86159 Augsburg, Germany
kerstin.dittmann@mrm.uni-augsburg.de

Abstract: *The metallic glass presented in this work with alloy composition $Ni_{60}Nb_{20}Ta_{20}$ (at.-%) obtained its amorphous structure through a powder atomization process and was processed into an open-porous foam using laser powder bed fusion. Subsequently, the open-porous structure was infiltrated with an AlSi12 eutectic aluminum alloy by gas pressure infiltration. For manufacturing processes and applications, knowledge of thermal properties of the metallic glass foam as well as metal matrix composite is essential. Therefore, characteristics of thermal expansion were determined experimentally by dilatometry, specific heat capacity by differential scanning calorimetry and thermal conductivity by laser flash analysis. Thermal expansion as well as specific heat capacity are measured for the metallic glass foam as well as infiltrated composite. Laser flash analysis method was applied to the infiltrated composite only, as this method is not suitable for an open-porous structure. Thermal investigations revealed a relaxation in the metallic glass, which was investigated in detail.*

Keywords: metallic glass; metal matrix composite; thermal expansion; specific heat capacity; thermal conductivity

1. Introduction

Compared to crystalline metals, metallic glasses exhibit remarkable properties such as high strength, hardness, elastic strain limit due to their amorphous structure [1–3]. Conversely, they also exhibit low toughness and high susceptibility to brittle fracture, making them less qualified for the use as monolithic structural components [4]. To compensate for brittleness, metallic glasses are increasingly used as a reinforcing phase in a hybrid material, such as metal matrix composites (MMC) with interpenetrating structures. This requires that the metallic glass has an open-porous foam structure so that it can be infiltrated with a metal that has more ductile properties [5, 6]. The metallic glass used in this work with alloy composition $Ni_{60}Nb_{20}Ta_{20}$ (at.-%) obtained its amorphous structure through a powder atomization process and was processed into an open-porous foam using laser powder bed fusion (LPBF). Subsequently, the open-porous structure was infiltrated with an AlSi12 eutectic aluminum alloy by gas pressure infiltration. Due to the high crystallization temperature of the metallic glass $Ni_{60}Nb_{20}Ta_{20}$ alloy (721 °C [7]) and the low melting temperature of the AlSi12 alloy (577 °C [8]), it was possible to select a corresponding process temperature of 660 °C to maintain the amorphous structure of the metallic glass. For manufacturing processes and applications, the knowledge of thermal properties of the metallic glass foam as well as the MMC is essential. Therefore, the characteristics of thermal expansion were determined experimentally and characterized by dilatometer measurements, specific heat capacity by differential scanning calorimetry (DSC) and

 ©2022 Dittmann et al. doi:10.5075/epfl-298799_978-2-9701614-0-0 published under CC BY-NC 4.0 license

thermal conductivity by laser flash analysis (LFA). The thermal expansion as well as specific heat capacity are measured and investigated on the metallic glass foam as well as on the infiltrated composite. The LFA method was applied to the infiltrated composite only, as this method is not suitable for an open-porous structure. In addition, the thermal investigations revealed a relaxation in the metallic glass, which was also investigated in detail. Metallic glasses are formed by supercooling a liquid melt at very high cooling rates (10^2-10^8 K/s) [9, 10]. During this process, free volume is frozen, and the metallic glass is in a thermodynamic metastable state. Upon reheating (below crystallization temperature), a relaxation process begins. Thermally activated diffusion closes the free volume and a thermodynamic equilibrium is reached [11–13].

2. Material and experimental methods

2.1 Material

The metallic glass presented in this work with an alloy composition $Ni_{60}Nb_{20}Ta_{20}$ (TaNi39.1Nb20.7 wt.-%) obtained its amorphous structure through a gas atomization process by the company Nanoval GmbH & Co.KG (Berlin, Germany). The Nanoval process is crucible-free [14] and was carried out in an inert argon atmosphere. Rapid cooling causes the material to solidify into an amorphous powder with particle size $d_{50} = 44\,\mu m$. The powder was further processed into an open-porous foam with a measured reinforcement volume fraction of 37.7 % using LPBF. This Process was conducted by the research group “Production and Component Behavior” at the Institute for Applied Materials – Materials Science and Engineering, Karlsruhe Institute of Technology. Subsequently, the open-porous structure was infiltrated with an AlSi12 eutectic aluminum alloy by gas pressure infiltration. Due to the high crystallization temperature of the metallic glass $Ni_{60}Nb_{20}Ta_{20}$ alloy (721 °C [7]) and the low melting temperature of the AlSi12 alloy (577 °C [8]), a corresponding process temperature of 660 °C was selected to maintain the amorphous structure of the metallic glass. This results in an interpenetrating MMC with metallic glass as reinforcement phase.

2.2 Experimental methods

Investigations on thermal expansion of the $Ni_{60}Nb_{20}Ta_{20}$ open-porous foam, the infiltrated MMC as well as the AlSi12 for comparison were carried out in a dilatometer type DIL 402 Expedis from Netzsch (Selb, Germany). The examined samples were cuboid-shaped with dimensions of $5 \times 5 \times 10\,mm^3$ and plane-parallel surfaces. Due to the different structure of the $Ni_{60}Nb_{20}Ta_{20}$ open-porous foam along and across the building direction caused by the LPBF process, the material is investigated in both directions regarding thermal expansion. Figure 1 shows on the

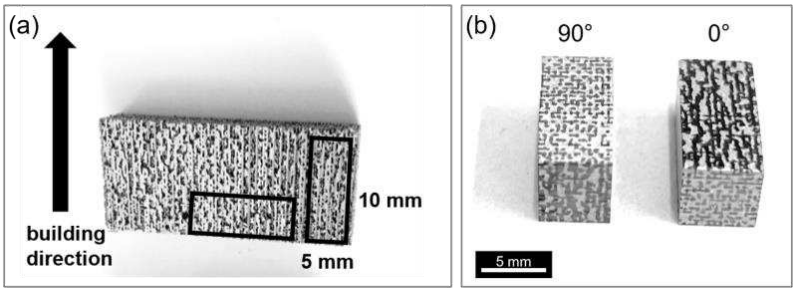

Figure 1. Samples for dilatometer measurements parallel (0°) and perpendicular (90°) to building direction. (a) Samples of $Ni_{60}Nb_{20}Ta_{20}$ open-porous foam. (b) Samples of infiltrated MMC with AlSi12.

 ©2022 Dittmann et al. doi:10.5075/epfl-298799_978-2-9701614-0-0 published under CC BY-NC 4.0 license

left side the $Ni_{60}Nb_{20}Ta_{20}$ open-porous foam and on the right side the MMC infiltrated with AlSi12.Measurements parallel to building direction are identified with 0° and perpendicular to building direction with 90°. Three thermal cycles of 20 °C to 500 °C with a constant heating and cooling rate of 5.5 K/min were carried out for each sample. The upper temperature limit was chosen to remain below crystallization temperature of the metallic glass and melting temperature of the AlSi12 (577 °C [8]). The contact force was set to 0.2 mN. To avoid oxidation all measurements were performed in an inert argon atmosphere. Therefore, the dilatometer was evacuated to a vacuum of 10^{-4} mbar and purged three times with argon to minimize the residual oxygen content. A reference measurement was performed with a Al_2O_3 sample to eliminate any effects of the testing device. All measurements were carried out and evaluated according to DIN 51045-1. The coefficients of thermal expansion (CTE) were evaluated in a range of 60 °C to 480 °C.

The specific heat capacity was determined by means of dynamic differential calorimetry in a DSC 214 Polyma from Netzsch (Selb, Germany) according to DIN 51007. For comparison and validation of the results, an Al_2O_3 sample was again used as reference. Accordingly, a sample size of approximately 1 x 2 x 3 mm³ of the $Ni_{60}Nb_{20}Ta_{20}$ foam and the MMC was chosen. The temperature program for the heat capacity measurements is composed of an isothermal start phase at 0 °C, a dynamic phase with constant heating rate of 20 K/min up to 200 °C and a final isothermal end phase at 200 °C. Since relaxation in metallic glasses has an influence on the specific heat capacity, the relaxation temperature T_r was first determined. For this purpose, four DSC measurements from ambient temperature to 500 °C (20 K/min) were carried out on one sample. All measurements were performed in an inert argon atmosphere.

Thermal conductivity was determined using laser flash analysis. The measurements were carried out with a LFA 1000 of the company Linseis (Selb, Germany) according to ASTM E 1461. In this method, the thermal diffusivity (a) of the material is measured, and the thermal conductivity (λ) is calculated with the density (ρ) and specific heat capacity (c_p) using equation 1.

$$\lambda = a\rho c_p \tag{1}$$

The specimens must have plane-parallel top and bottom surfaces and a defined thickness. This resulted in a specimen size of 10 x 10 x 1.6 mm³ as shown in Figure 2.

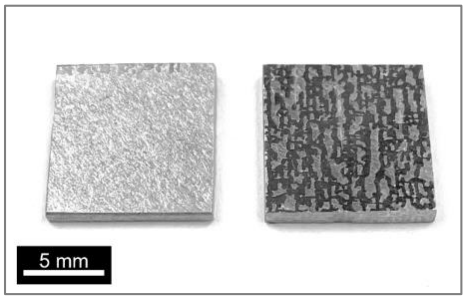

Figure 2. Samples for LFA. Left: Sample of AlSi12. Right: Sample of the infiltrated MMC.

Furthermore, the measurements require a continuous sample body, which is why the $Ni_{60}Nb_{20}Ta_{20}$ open-porous foam could not be investigated with this method. Therefore, the measurement was additionally performed on an AlSi12 sample for comparison.

 ©2022 Dittmann et al. doi:10.5075/epfl-298799_978-2-9701614-0-0 published under CC BY-NC 4.0 license

3. Results

3.1 Thermal expansion

Figure 3 shows the temperature-dependent evolution of the thermal strain during the three thermal cycles of the $Ni_{60}Nb_{20}Ta_{20}$ open-porous foam (Fig.3 (a)), the infiltrated MMC $Ni_{60}Nb_{20}Ta_{20}$-AlSi12 (Fig.3 (b)), and for comparison of the AlSi12 matrix itself (Fig. 3 (c)).

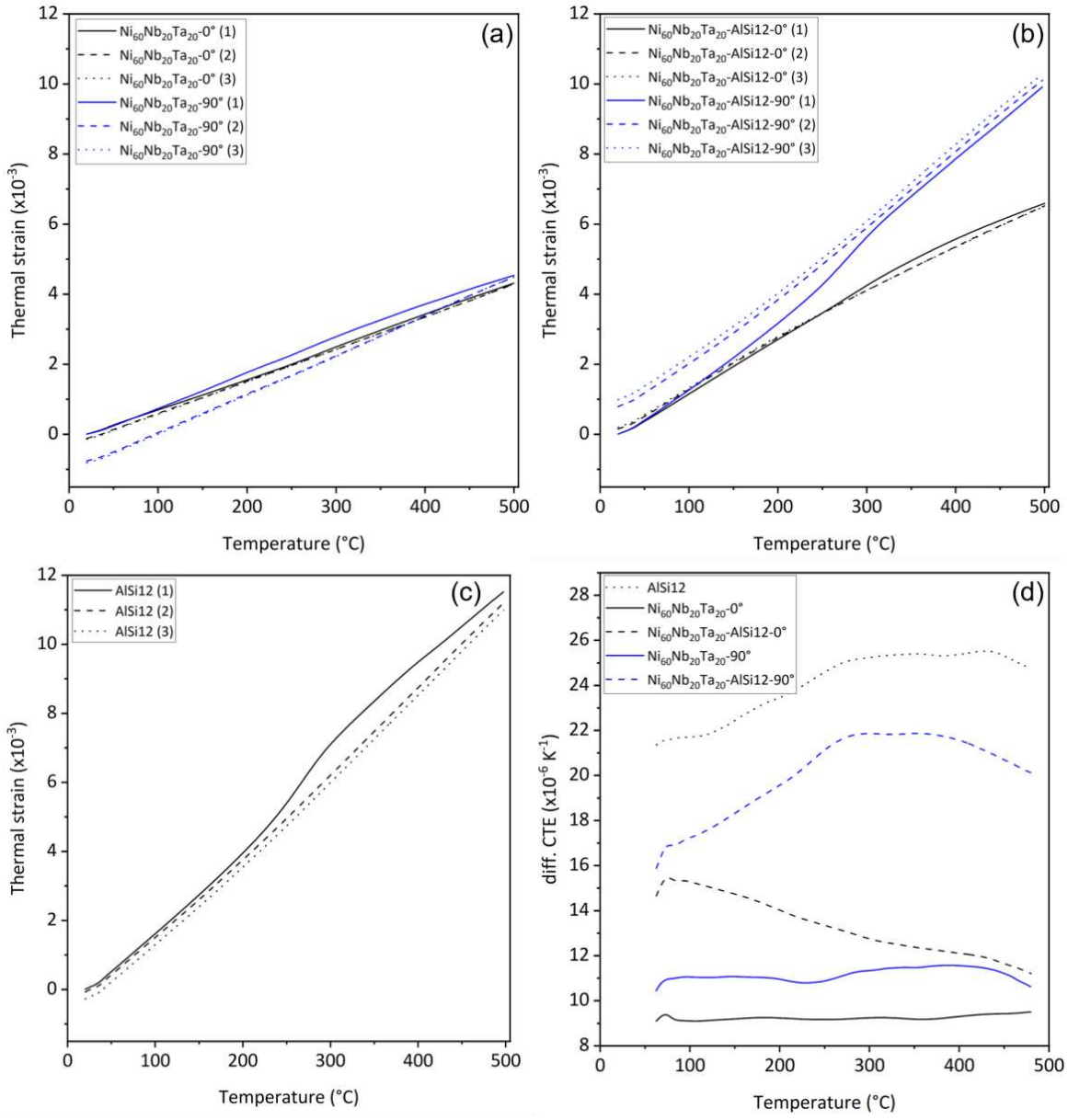

Figure 3. Results of dilatometer measurements. (a) Thermal strain of $Ni_{60}Nb_{20}Ta_{20}$ open-porous foam in 0° and 90° direction. (b) Thermal strain of infiltrated MMC $Ni_{60}Nb_{20}Ta_{20}$-AlSi12 in 0° and 90° direction. (c) Thermal strain of AlSi12. (d) Differential CTE results for all samples.

The first heating cycle of all samples exhibit a distinct increase starting at 200 °C, whereas the following second and third cycle are on the same track. The $Ni_{60}Nb_{20}Ta_{20}$ open-porous foam exhibits with 0.43 % in 0°- and 0.45 % in 90°-direction nearly the same expansion in both directions. However, the sample in 90°-direction shows some remaining negative thermal strain after the cycles, as do the sample of AlSi12. AlSi12 exhibits a max. thermal strain of 1.11 %. The

 ©2022 Dittmann et al. doi:10.5075/epfl-298799_978-2-9701614-0-0 published under CC BY-NC 4.0 license

infiltrated MMC combines metallic glass $Ni_{60}Nb_{20}Ta_{20}$ and AlSi12 and results in a max. thermal strain of 0.66 % in 0°-direction and 1.0 % in 90°-direction. Additionally, the samples in 90°-direction exhibit a positive remaining negative thermal strain after the second and third heating cycle. The increase in the first cycle can be attributed to relaxation in the metallic glass [11] and to an internal stress generated in MMCs during solidification at manufacturing process [15]. In order to exclude these influences, only the average value from the second and third heating process is considered in the analysis of CTEs shown in Figure 3 (d). The determined CTE of the metallic glass $Ni_{60}Nb_{20}Ta_{20}$-0° is constant value of $(9.24 \pm 0.10) \times 10^{-6} K^{-1}$ with increasing temperature. The CTE of $Ni_{60}Nb_{20}Ta_{20}$-90° remains nearly the same at $(11.17 \pm 0.26) \times 10^{-6} K^{-1}$ with a small increase starting at 250 °C. In contrast, the CTEs of the MMC as well as the matrix material AlSi12 are not linear with increasing temperature. The CTE of the $Ni_{60}Nb_{20}Ta_{20}$-AlSi12 in 0°-direction decreases with increasing temperature from $(14.65 \pm 0.19) \times 10^{-6} K^{-1}$ at 60 °C to $(11.21 \pm 0.96) \times 10^{-6} K^{-1}$ at 480 °C. Whereas, the CTE of the $Ni_{60}Nb_{20}Ta_{20}$-AlSi12-90° is $(15.88 \pm 0.32) \times 10^{-6} K^{-1}$ at 60 °C and increases to a maximum of approx. $21 \times 10^{-6} K^{-1}$ at 300 °C. Subsequently, the value decreases again to $(20.12 \pm 0.94) \times 10^{-6} K^{-1}$ at 480 °C. Similar behavior is observed for the AlSi12-matrix. The CTE starts with $(21.35 \pm 0.25) \times 10^{-6} K^{-1}$, increases to a maximum of approx. $25 \times 10^{-6} K^{-1}$ between 300 - 400 °C and decreases to $(24.72 \pm 2.88) \times 10^{-6} K^{-1}$.

3.2 Specific heat capacity and relaxation

In order to obtain a specific heat capacity independent of the thermal history of the material, an upper temperature limit was first determined experimentally using DSC measurements (Fig. 4 (b)). The DSC signals of the first heating cycle differs from the three following ones.

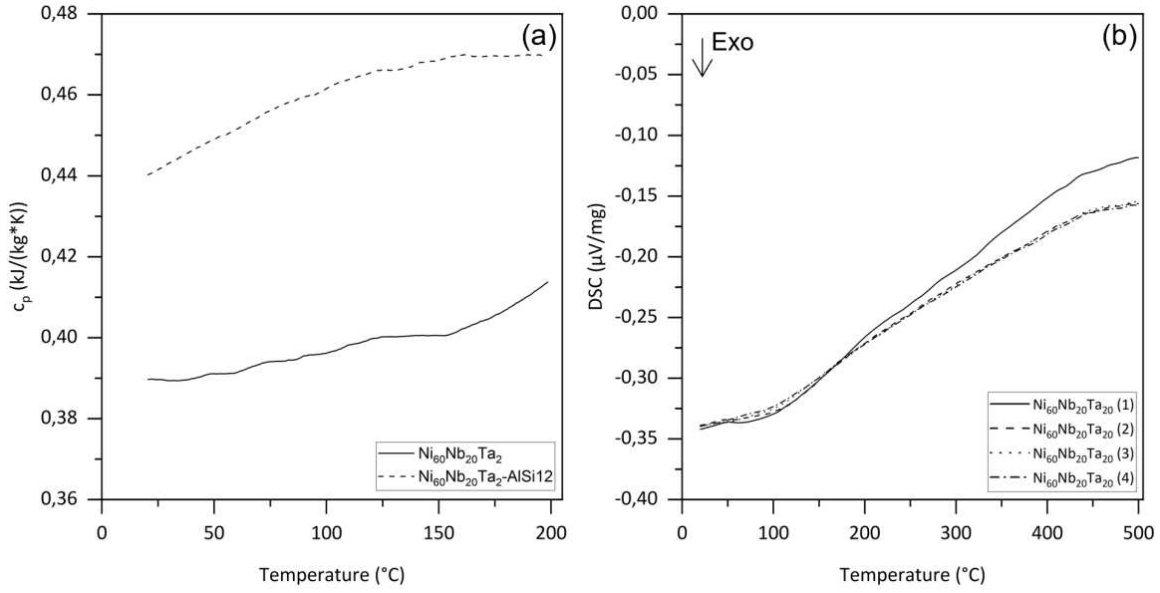

Figure 4. Results of DSC measurements. (a) Specific heat capacity of $Ni_{60}Nb_{20}Ta_{20}$ open-porous foam MMC $Ni_{60}Nb_{20}Ta_{20}$-AlSi12. (b) DSC signal of $Ni_{60}Nb_{20}Ta_{20}$ open-porous foam.

The relaxation temperature T_r therefore corresponds to the temperature at which the DSC signals start to diverge at approximately 200 °C. Consequently, this value was chosen as upper temperature limit for the determination of the specific heat capacity of the metallic glass $Ni_{60}Nb_{20}Ta_{20}$ and the MMC $Ni_{60}Nb_{20}Ta_{20}$-AlSi12 (Fig. 4 (a)). Both c_p values increase with increasing temperature. $Ni_{60}Nb_{20}Ta_{20}$ starts at 0.39 ± 0.01 kJ/kgK at ambient temperature (20 °C) and

increases until 0.42 ± 0.01 kJ/kgK at 200 °C. Whereas, the MMC $Ni_{60}Nb_{20}Ta_{20}$-AlSi12 starts with a much higher value at 0.44 ± 0.01 kJ/kgK at 20 °C and increases until 0.47 ± 0.01 kJ/kgK at 200 °C.

3.3 Thermal conductivity

For the evaluation of the AlSi12 sample a density of 2640 kg/m³ and a heat capacity of 0.90 kJ/kgK was used according to literature [16], with a measured thermal diffusivity of $(0.65 \pm 0.02) \times 10^{-4}$ m²/s resulting in a thermal conductivity of 154.43 ± 4.21 W/mK. The thermal conductivity of the infiltrated MMC $Ni_{60}Nb_{20}Ta_{20}$-AlSi12 is 59.44 ± 1.01 W/mK and was calculated with a measured density of 5690 kg/m³, the result of the investigated heat capacity of 0.44 kJ/kgK at ambient temperature and a measured thermal diffusivity of $(0.24 \pm 0.01) \times 10^{-4}$ m²/s. All results are summarized in Table 1.

Table 1. Results of thermal conductivity measured by LFA.

Material	ρ (kg/m³)	$c_{p,20°C}$ (kJ/kgK)	a ($\times 10^{-4}$ m²/s)	λ (W/mK)
AlSi12	2640 [8]	0.90 [16]	0.65 ± 0.02	154.43 ± 4.21
$Ni_{60}Nb_{20}Ta_{20}$	10790	0.39 ± 0.01	-	-
$Ni_{60}Nb_{20}Ta_{20}$-AlSi12	5690	0.44 ± 0.01	0.24 ± 0.01	59.44 ± 1.01

4. Discussion

The results show that the thermal expansion of the two components of the MMC differ strongly. Whereas the AlSi12 has a high max. thermal strain of 1.11 % and CTE of 21 to 25×10^{-6} K^{-1}, which corresponds with literature [17, 18], the metallic glass $Ni_{60}Nb_{20}Ta_{20}$ exhibits a significantly lower max. thermal strain of 0.43 % and 0.45 % and CTE of 9 to 11×10^{-6} K^{-1}. There is no data published for the metallic glass $Ni_{60}Nb_{20}Ta_{20}$ yet, but an estimation according to [19] leads to an approx. CTE of 8.97×10^{-6} K^{-1} by using the glass transition temperature $T_g = 936$ K of the same composition in [20], which confirms the results. The metallic glass shows an increase in thermal expansion during the first heating cycle starting at 200 °C, due to thermal relaxation as confirmed by the DSC measurements. In addition, a slight anisotropy between the sample parallel (0°) and perpendicular (90°) to building direction is apparent. AlSi12 also shows an increase during the first heating cycle, starting at 300 °C, which suggests that internal residual stresses already exist in the material. MMC with components whose CTE differ greatly exhibit thermal residual stresses after manufacturing. These are generally expected to be compressive stresses in the reinforcement phase and tensile stresses in the matrix when the CTE of the matrix material is higher than the CTE of the reinforcement phase [15, 21]. All these effects combined lead to the resulting thermal expansion of the MMC $Ni_{60}Nb_{20}Ta_{20}$-AlSi12. Due to the structure of the $Ni_{60}Nb_{20}Ta_{20}$ open-porous foam, the samples exhibit anisotropy in 0°- and 90°-direction. This is further enhanced by the different component proportions in the respective directions. The properties of the metallic glass dominate in 0°- and of the AlSi12 in 90°-direction. Therefore, the MMC in 90°-direction has a significantly higher thermal expansion of 1.0 % than the MMC in 0°-direction with 0.66 %. The anisotropy in the CTE is equally evident. The AlSi12 dominated MMC (90°) behaves similarly to the CTE of AlSi12 and increases from 15 to 21×10^{-6} K^{-1}, with increasing temperature. Whereas the metallic glass dominated MMC (0°) decreases linearly from 14 to 11×10^{-6} K^{-1}, and thus a linear behavior more typical for metallic glasses [19]. All thermal

 ©2022 Dittmann et al. doi:10.5075/epfl-298799_978-2-9701614-0-0 published under CC BY-NC 4.0 license

expansion results are consistent with results of a MMC with $Ni_{60}Nb_{20}Ta_{20}$ as particle reinforcement phase in literature [18].
The resulted specific heat capacity show that AlSI12 with 0.90 kJ/kgK (20 °C) combined with $Ni_{60}Nb_{20}Ta_{20}$ with 0.39 kJ/kgK (20 °C) increases the c_p of the MMC to 0.44 kJ/kgK. The c_p of the metallic glass has not yet been determined, which is why there are no comparative values. However, if the value is compared with the c_p of the individual components ($c_{p,Ni}$ = 0.45 kJ/kgK, $c_{p,Nb}$ = 0.26 kJ/kgK, $c_{p,Ta}$ = 0.14 kJ/kgK [16]), it can be seen that the values correspond well and lead to the conclusion that the results of the MMC also appear realistic.
Same applies to the heat capacity of the MMC, no comparable literature values are yet available. However, the result of the AlSi12 shows that the method provides realistic results, since 154 W/mK corresponds to literature [8, 16]. Considering that nickel (67 W/mK), niobium (54 W/mK) and tantalum (54 W/mK) [16] have a significantly lower thermal conductivity than AlSi12, it can be concluded that the results of the MMC with 59 W/mK appear realistic.

5. Conclusion

A metallic glassy $Ni_{60}Nb_{20}Ta_{20}$ open-porous foam and infiltrated MMC were successfully investigated in terms of thermal expansion, specific heat capacity and thermal conductivity. Thermal expansion was investigated parallel (0°) and perpendicular (90°) to building direction and a pronounced anisotropy was determined. Samples in 90°-direction exhibit a significantly higher thermal expansion with increasing temperature than samples in 0°-direction. The determined heat capacity and thermal conductivity also provide new values for the metallic glass $Ni_{60}Nb_{20}Ta_{20}$ as well as the MMC.

Acknowledgements

The authors are especially thankful to Steffen Czink from the research group "Production and Component Behavior" at the Institute of Applied Materials - Materials Science and Engineering, Karlsruhe Institute of Technology for carrying out the LPBF procedure. Also, special thanks to R. Horny and M. Belli for their technical and experimental support. The financial support of the German Research Foundation (DFG) within the project WE 4273/19-1 is gratefully acknowledged.

6. References

[1] Inoue A, Shen B, Koshiba H, Kato H, Yavari AR. Cobalt-based bulk glassy alloy with ultrahigh strength and soft magnetic properties. Nat. Mater. 2003; 2(10): 661–3 [https://doi.org/10.1038/nmat982]
[2] Inoue A, Shen BL, Chang CT. Fe- and Co-based bulk glassy alloys with ultrahigh strength of over 4000MPa. Intermetallics 2006; 14(8-9): 936–44 [https://doi.org/10.1016/j.intermet.2006.01.038]
[3] Schroers J. Processing of bulk metallic glass. Adv. Mater. 2010; 22(14): 1566–97 [https://doi.org/10.1002/adma.200902776]
[4] Ashby M, Greer A. Metallic glasses as structural materials. Scr. Mater. 2006; 54(3): 321–6 [https://doi.org/10.1016/j.scriptamat.2005.09.051]
[5] Zhang H, Wang A, Li H*, et al.* Quasi-static compressive property of metallic glass/porous tungsten bi-continuous phase composite. J. Mater. Res. 2006; 21(6): 1351–4 [https://doi.org/10.1557/jmr.2006.0166]

 ©2022 Dittmann et al. doi:10.5075/epfl-298799_978-2-9701614-0-0 published under CC BY-NC 4.0 license

[6] Sun Y, Zhang HF, Wang AM*, et al.* Mg-based metallic glass/titanium interpenetrating phase composite with high mechanical performance. Appl. Phys. Lett. 2009; 95(17): 171910 [https://doi.org/10.1063/1.3257699]
[7] Lee M, Bae D, Kim W, Kim D. Ni-based refractory bulk amorphous alloys with high thermal stability. Mater. Trans. 2003; 44(10): 2084–7 [https://doi.org/10.2320/matertrans.44.2084]
[8] Mondolfo LF. Aluminum alloys: Structure and properties. London and Boston: Butterworths 1976.
[9] Johnson WL. Bulk glass-forming metallic alloys: Science and technology. MRS Bull. 1999; 24(10): 42–56 [https://doi.org/10.1557/S0883769400053252]
[10] Inoue A, Takeuchi A. Recent development and application products of bulk glassy alloys. Acta Mater. 2011; 59(6): 2243–67 [https://doi.org/10.1016/j.actamat.2010.11.027]
[11] Egami T. Structural relaxation in metallic glasses. Ann. N. Y. Acad. Sci. 1981; 371: 238–51 [https://doi.org/10.1111/j.1749-6632.1981.tb55664.x]
[12] van den Beukel A, Radelaar S. On the kinetics of structural relaxation in metallic glasses. Acta Mater. 1983; 31(3): 419–27 [https://doi.org/10.1016/0001-6160(83)90219-5]
[13] Tiwari G, Ramanujan R, Gonal M*, et al.* Structural relaxation in metallic glasses. Mater. Sci. Eng. A 2001; 304-306: 499–504 [https://doi.org/10.1016/S0921-5093(00)01503-3]
[14] DDMC2018 Fraunhofer Direct Digital Manufacturing Conference: Proceedings. Stuttgart: Fraunhofer Verlag; 2018.
[15] Huber T, Degischer HP, Lefranc G, Schmitt T. Thermal expansion studies on aluminium-matrix composites with different reinforcement architecture of SiC particles. Compos. Sci. Technol. 2006; 66(13): 2206–17 [https://doi.org/10.1016/j.compscitech.2005.12.012]
[16] GRANTA EduPack; 2020.
[17] Roy S, Nagel A, Weidenmann KA. Anisotropic thermal expansion behavior of an interpenetrating metal/ceramic composite. Thermochim. Acta 2020; 684: 178488 [https://doi.org/10.1016/j.tca.2019.178488]
[18] Lichtenberg K, Weidenmann KA. Effect of reinforcement size and orientation on the thermal expansion behavior of metallic glass reinforced metal matrix composites produced by gas pressure infiltration. Thermochim. Acta 2017; 654: 85–92 [https://doi.org/10.1016/j.tca.2017.05.010]
[19] Kato H, Chen H-S, Inoue A. Relationship between thermal expansion coefficient and glass transition temperature in metallic glasses. Scr. Mater. 2008; 58(12): 1106–9 [https://doi.org/10.1016/j.scriptamat.2008.02.006]
[20] Lichtenberg K. Metallmatrixverbunde mit Verstärkungselementen aus metallischem Glas Ni60Nb20Ta20: Herstellung und Charakterisierung. Dissertation Karlsruhe Institute of Technology 2017.
[21] Bourke M, Goldstone JA, Stour MG, Needleman A. Characterization of Residual Stresses in Composites. In: Fundamentals of Metal-Matrix Composites. Elsevier 1993; 61–80.

 ©2022 Dittmann et al. doi:10.5075/epfl-298799_978-2-9701614-0-0 published under CC BY-NC 4.0 license